

# Drivers of day-night intra-surface urban heat island variations under local extreme heat: A case study of Singapore

Siyu Li<sup>a</sup>, Filip Biljecki<sup>a,b</sup>, Pengyuan Liu<sup>c,d</sup>, Rudi Stouffs<sup>a,\*</sup>

<sup>a</sup>*Department of Architecture, National University of Singapore, Singapore*

<sup>b</sup>*Department of Real Estate, National University of Singapore, Singapore*

<sup>c</sup>*Future Cities Lab Global, Singapore-ETH Centre, Singapore*

<sup>d</sup>*Urban Analytics Subject Group, Urban Studies & Social Policy Division, University of Glasgow, United Kingdom*

## Abstract

Urban areas face significant challenges from extreme heat and urban heat islands (UHIs), which often interact and intensify each other at multi-spatial scales. However, most existing studies examine extreme heat and its interaction with UHIs at the city scale, overlooking the spatial heterogeneity of temperature responses within local areas. Extreme heat does not manifest uniformly across the entire city, and the UHI is a typically localized phenomenon influenced by changes in local climate and urban factors. To address this gap, this study defines local extreme heat (LEH) at the local scale based on 1 km and examines surface urban heat island (SUHI) response to local extreme heat (LEH) in Singapore, a tropical city experiencing more frequent extreme heat events. Using multi-year temperature datasets, we calculated the difference in SUHI intensity (SUHII) between LEH and non-LEH conditions, referred to as  $\delta$ SUHII. Our findings revealed that SUHII responses to LEH differed by daytime and nighttime and local areas. Daytime  $\delta$ SUHII peaked at 3.2°C in the northeast, while nighttime  $\delta$ SUHII reached 0.6°C in other regions. To identify the dominant drivers of SUHII responses to LEH, we employed the spatial Random Forest (spatialRF) model. Our results showed that the spatialRF model achieved R-squared values exceeding 63% for predicting daytime  $\delta$ SUHII and 45% for nighttime  $\delta$ SUHII. LEH, land use, and vegetation dominantly contributed to daytime  $\delta$ SUHII, while socioeconomic factors mostly influenced nighttime  $\delta$ SUHII. Furthermore, we applied SHAP to interpret the spatialRF model. Hotspots of

\*Corresponding author

both daytime and nighttime  $\delta$ SUHII were driven by socio-economic factors. Finally, non-linear associations showed that the cooling effect of vegetation reached saturation, as the SHAP values remained positive, while water bodies, as indicated by a U-shaped SHAP pattern followed by a decline, were more effective in mitigating SUHII increases under LEH conditions.

*Keywords:* Local extreme heat, Surface urban heat island, Building and environmental factors, Socioeconomic factors, Local scale

---

## 1. Introduction

Urban areas are experiencing overheating caused by both the challenges of urban heat islands (UHIs) and extreme heat nowadays. Specifically, extreme heat occurs more frequently due to global climate change, and UHIs are considered to be one of the major problems posed to humans in the 21st century (Rizwan et al., 2008). Urban overheating caused by either UHIs or extreme heat has led to serious dual damage to human health and the environment, causing heat-related deaths (Dai and Liu, 2022; Ho et al., 2023; Shahmohamadi et al., 2011; Tan et al., 2010) and excessive energy consumption (Singh and Sharston, 2022; Hirano and Fujita, 2012).

The urban heat island (UHI) and extreme heat can interact at multi-spatial scales, showing amplification, reduction, or no change in UHI intensity (UHII). Most studies have investigated city-scale UHI intensity (UHII) changes by extreme heat events (Zhao et al., 2018; Li and Bou-Zeid, 2013; He et al., 2020; Rizvi et al., 2019; Syed Mahbar and Kusaka, 2024). For example, UHII increases during extreme heat during the day in U.S. cities (Zhao et al., 2018) and at night in Australian cities (Rogers et al., 2019), but decreases in inland cities of Paris (Shreevastava et al., 2021) and remains unchanged in the city of Dijon, France (Richard et al., 2021). Typically, UHI is the localized phenomenon influenced by changes in local climate and urban factors such as land use, built structures, green and blue infrastructure, and construction materials (Oke et al., 2017; He et al., 2021; Cui et al., 2023). Some studies have explored intra-UHII variations during extreme heat periods compared to non-extreme heat periods. For example, weather stations located in high-rise building areas in Guangzhou, China, revealed significant interactions between

temperature and UHI, with shading playing a key role (Luo et al., 2023). Similarly, urban parks were found to have the lowest UHII during the extreme heat period in Hannover, Germany (Kabisch et al., 2023). However, these studies typically identified extreme heat events at the city scale, overlooking the spatial heterogeneity of temperature responses within cities, as extreme heat does not always uniformly occur across the entire city. Extreme heat has been mostly explored at the regional (Perkins-Kirkpatrick and Gibson, 2017) and city (He et al., 2025; Su et al., 2025). Especially, extreme heat can vary significantly across different local areas within a city, as few studies have highlighted Yu et al. (2023); Cui et al. (2023). For instance, Yu et al. (2023) provided evidence that extreme heat events occurred more frequently in the northeastern areas of Singapore. Another study of (Cui et al., 2023) showed that different LCZs exhibit various characteristics of intensity, frequency, and duration of extreme heat events found in Beijing, China. This highlights the need to consider the spatial heterogeneity of extreme heat within a city.

By considering that the UHI is typically a localized phenomenon, and it is essential to consider extreme heat at the local scale, to address this, local extreme heat (LEH) is defined in this study based on 1 km spatial units. Furthermore, extreme heat and UHI may interact at the local scale, potentially leading to amplified intra-UHII under LEH conditions; however, the localized synergies between UHI and extreme heat remain unclear. Most previous studies on UHI and extreme heat interactions rely heavily on weather station data (He et al., 2021; Hathway and Sharples, 2012; Cui et al., 2023), which limits spatial coverage and makes it difficult to fully capture intra-urban heterogeneity in UHI and extreme heat patterns. Satellite data provides the advantage of complete spatial coverage, enabling the generation of seamless near-surface air temperature and land surface temperature datasets. This offers a valuable opportunity to comprehensively explore the spatial patterns of localized synergy between UHI and extreme heat. Accordingly, this study focuses on surface urban heat island (SUHI) and investigates SUHII responses to LEH, which is defined as the difference in SUHI intensity (SUHII) between LEH and non-LEH conditions.

In addition, most studies have employed physical numerical weather prediction (NWP)

models to explore the drivers of UHI-extreme heat interactions (Chen et al., 2023; Mag-naye and Kusaka, 2024). A key component of NWP is the urban canopy model (UCM), which requires detailed datasets (e.g., LULC, building height, satellite/LiDAR data) and substantial computational resources (Lauer et al., 2023; Li et al., 2019; Rajeswari et al., 2024). However, data scarcity and high computational demands often limit their application (He et al., 2020; Li and Bou-Zeid, 2013). Statistical methods have also been used for their efficiency and generalization (Luo et al., 2023), but conventional regression and correlation cannot fully capture the complexity of the interactions between variables. Recently, interpretable machine learning (ML) techniques have emerged as efficient and generalizable alternatives (Yang et al., 2022; He et al., 2024). SHapley Additive Explanations (SHAP) quantify the contribution of each feature to model predictions, and models such as Random Forest (RF) and XGBoost have been widely applied. However, these conventional models do not account for spatial autocorrelation. SpatialRF addresses this limitation by incorporating spatial structure, reducing residual autocorrelation, and providing more reliable variable importance scores (Benito, 2021a; Yang et al., 2024).

Building on this, our study applies an interpretable SpatialML framework to the study area of Singapore, a high-density tropical city, to identify the dominant drivers of SUHII responses to LEH. We conceptualize LEH as not simply treated as a background climatic factor; rather, variations in LEH, such as intensity, frequency, and duration of LEH, can impact SUHII in local areas. Urban factors serve as preexisting factors that can modulate the level of UHII changes caused by LEH. Accordingly, this study examines urban morphology, land use, socioeconomic conditions, and LEH characteristics to identify the key drivers of SUHII responses. Specifically, this study addresses the following questions:

- What is the spatial pattern of daytime and nighttime SUHII responses to LEH in Singapore?
- What are the key drivers of daytime and nighttime SUHII responses to LEH for Singapore?

- What are the dominant drivers of daytime and nighttime SUHII responses to LEH in different areas of Singapore, and what spatial patterns do they exhibit?

By addressing the above research questions, this study proposes an analytical framework for exploring SUHII responses to LEH and its underlying drivers from global and local perspectives. The developed framework can be applied to other cities, offering insights into sustainable urban planning and environmental policymaking for tropical high-density cities facing increasing heat challenges.

## 2. Material and methodology

This study proposes an analytical workflow to investigate the spatial pattern and drivers of SUHII responses to LEH, as shown in [\[1\]](#). The framework contains five cores: the first core is to identify LEH conditions and then calculate SUHII responses to LEH, which is the difference of SUHII between LEH and non-LEH conditions; the second core is feature engineering for the built and environmental, socioeconomic, and LEH features; the third core is to construct the spatial RF model; the fourth core is to identify dominant drivers for the city; and the fifth core is to employ the SHAP model to interpret spatialML to identify dominant drivers in local areas. The following sections introduce methods of the first core in [Section \[2.2\]](#) and [Section \[2.3\]](#), the second core in [Section \[2.4\]](#), the third and fourth cores in [Section \[2.5.1\]](#), and the fifth core in [Section \[2.5.2\]](#) and [Section \[2.5.3\]](#) in detail.

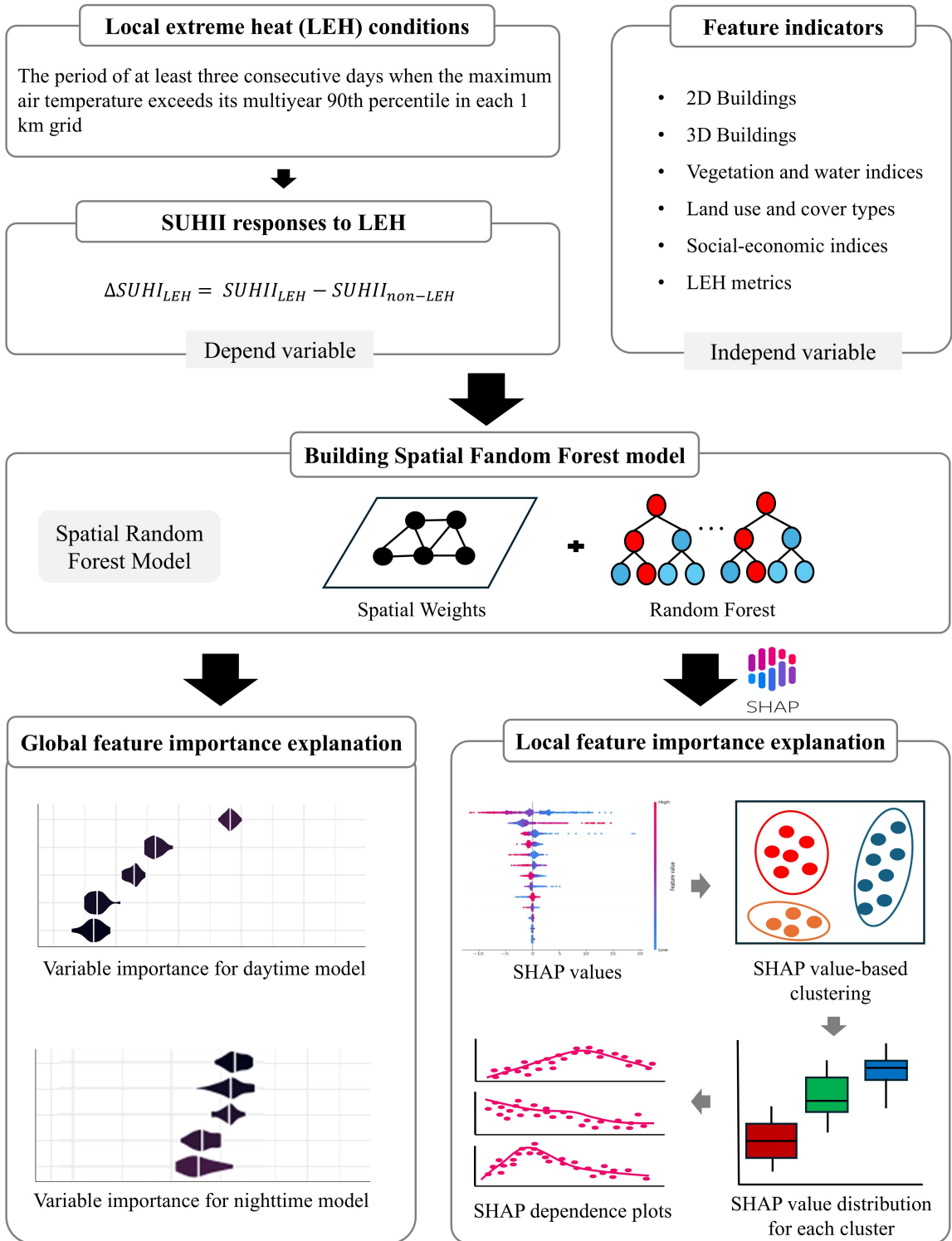


Figure 1: A proposed framework for investigating the spatial pattern and drivers of SUHII responses to LEH. The first part involves selecting LEH conditions and calculating the difference in SUHII between LEH and non-LEH conditions. The second part focuses on feature engineering, incorporating non-multicollinear features of 2D and 3D building metrics, natural indicators, land use types, socioeconomic variables, and LEH metrics. The third part constructs a spatial Random Forest (RF) model, where the SUHII response to LEH is the dependent variable, and non-multicollinear features serve as independent variables. The fourth part explores global feature importance to assess the key drivers of SUHII variation under LEH conditions for both daytime and nighttime. The fifth part investigates local feature importance through clustering and nonlinear analyses, aiming to reveal spatial heterogeneity in the influence of different features.

## 2.1. Study area and dataset

Singapore—a high-density tropical city—is selected as the case area to illustrate the proposed framework in this study. Singapore is located between 1°09' N and 1°29' N and 103°36' E and 104°25' E. Its climate type is a tropical rainforest climate (Köppen classification: Af) (Peel et al., 2007), characterized by no distinctive seasons, consistently high monthly average temperature (26–27.7°C), and an annual rainfall of approximately 2300 mm. Singapore's climate is characterized by two monsoon seasons separated by intermonsoonal periods. The Northeast Monsoon, occurring from December to early March, is associated with the highest monthly rainfall and weaker winds. The Southwest Monsoon, from June to September, corresponds to a relatively drier period (Meteorological Service Singapore, 2023). In Singapore, the diurnal temperatures and precipitation are more pronounced than the annual variation. The daily mean temperature typically ranges from a minimum of 23°C to 25°C to a maximum of 31°C to 33°C. Influenced by complex urban topography and the urban heat island effect, the difference in microclimate results in a significant spatial and temporal variation of ambient temperatures across Singapore, with differences reaching up to 3°C during daytime hours and 7°C at night (Yu et al., 2023).

This study utilized multiple datasets for Singapore. In order to identify LEH conditions, maximum near-surface air temperature ( $T_{\max}$ ) data was derived from the global gridded dataset of daily near-surface air temperature ( $T_a$ )<sup>1</sup> (Zhang et al., 2022), which provides daily observations at a 1 km resolution. To ensure comprehensive spatial coverage  $T_{\max}$  across Singapore, we selected  $T_{\max}$  for the years 2003, 2005, 2008, 2012, and 2019. Additionally, the land surface temperature (LST) data for daytime (1:30 pm) and nighttime (1:30 am) were obtained from the MODIS Gap-filled long-term land surface temperature dataset<sup>2</sup> (Zhang et al., 2021), with a spatial resolution of 1 km. We selected the daytime and nighttime LST for 2003, 2005, 2008, 2012, and 2019 to calculate the SUHII responses to LEH. Additionally, for factors considered in this study, Landsat images used in this study are USGS Landsat 8 Level 2, Collection 2, Tier 1 in 2019;

<sup>1</sup><https://gee-community-catalog.org/projects/airtemp/>

<sup>2</sup>[https://gee-community-catalog.org/projects/daily\\_lst/](https://gee-community-catalog.org/projects/daily_lst/)

USGS Landsat 7 Level 2, Collection 2, Tier 1 in 2012; and USGS Landsat 5 Level 2, Collection 2, Tier 1 in 2003, 2005, and 2008 for Singapore, which were retrieved from the Google Earth Engine. The 2019 Master Plan of Singapore and gross plot ratios (GPR) data were obtained from the Urban Redevelopment Authority. We used the Singapore 2019 Masterplan to retrieve land use types. Night-time light (NTL) data for 2003, 2005, 2008, 2012, and 2019 were sourced from global 500-meter resolution “NPP-VIRS-like” datasets (Chen et al., 2020), available from the National Earth System Science Data Centre, National Science & Technology Infrastructure of China. The building dataset, containing building shapes and height information extracted from digital surface model (DSM) data, was obtained from a previous study (ETH Zurich, 2024). Road data for Singapore was retrieved from OpenStreetMap. Additionally, the Global Artificial Impervious Area (GAIA) dataset (Version 2022) was used to extract impervious surface areas (Gong et al., 2020), and population density data at a 1 km resolution was acquired from the open-access WorldPop dataset.

## *2.2. Local extreme heat (LEH) and non-local extreme heat (non-LEH) conditions definition*

To identify LEH occurrences, we employed percentile-based thresholds based on multiple-year historical daily air temperature. The use of percentile-based thresholds is more effective than fixed absolute temperature thresholds when considering different urban thermal regimes within a city. The LEH condition is defined as the period lasting a minimum of three consecutive days during which the maximum air temperature ( $T_{\max}$ ) exceeds 90<sup>th</sup>  $T_{\max}$  percentile of the multi-year  $T_{\max}$  collection in each 1 km grid. This definition builds on concepts used to identify extreme heat events at weather station (Cui et al., 2023), block (Castro et al., 2024), and citywide scales (Coughlan de Perez et al., 2023; Wu et al., 2023). Correspondingly, the non-LEH condition is the days of LEH non-occurrence. A showcase of the schematic for identifying the LEH condition for one 1 km grid cell is shown in Fig. 2. Accordingly, LEH and non-LEH identification have been implemented in each 1 km grid cell within a city.

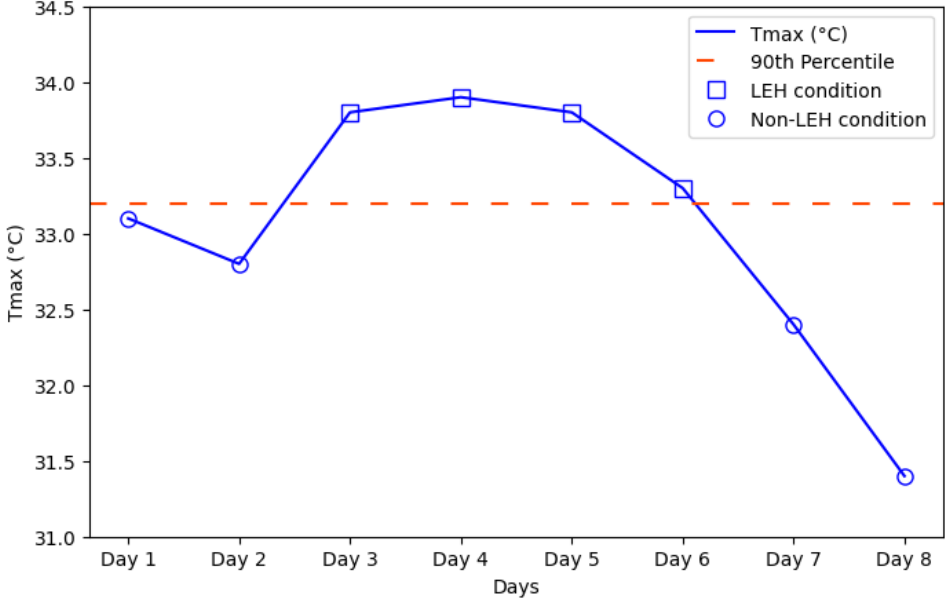


Figure 2: A showcase of the schematic of identifying LEH conditions based on daily  $T_{\max}$  (denoted by the blue line) and its corresponding 90<sup>th</sup> percentile values (denoted by the orange line) in one 1 km grid cell. LEH conditions are the days of  $T_{\max}$  exceeding its corresponding 90<sup>th</sup> percentile value (denoted by red dots). Conversely, non-LEH conditions refer to days without the occurrence of LEH conditions.

### 2.3. Surface urban heat island intensity (SUHII) calculation and SUHII responses to LEH

To explore the SUHII responses to LEH, the difference of SUHII between LEH and non-LEH conditions for each urban grid is calculated. Specifically, there are three main steps.

1. The daytime (or nighttime) SUHII under LEH conditions is calculated using Equations (1) and (2):

$$\text{SUHII}_t = \text{LST}_t - \frac{1}{M} \sum_{j=1}^M \text{LST}_{j,t} \quad (1)$$

$$\text{SUHII}_{\text{LEH}} = \frac{1}{T} \sum_{t \in T} \text{SUHII}_t \quad (2)$$

Where  $\text{LST}_t$  is the daytime (or nighttime) LST on the day  $t$ ,  $j$  represents rural grids,  $M$  is the total number of rural grids, and  $T$  is the number of days of LEH conditions.

2. The daytime (or nighttime) SUHII under non-LEH conditions is calculated using Equations (3) and (4):

$$\text{SUHII}_t = \text{LST}_t - \frac{1}{M} \sum_{j=1}^M \text{LST}_{j,t} \quad (3)$$

$$\text{SUHII}_{\text{non-LEH}} = \frac{1}{T'} \sum_{t \in T'_i} \text{SUHII}_t \quad (4)$$

Where  $\text{LST}_t$  is the daytime (or nighttime) LST on the day  $t$ ,  $j$  represents rural grids,  $M$  is the total number of rural grids, and  $T'$  is the number of days of non-LEH conditions.

3. The difference in daytime (or nighttime) SUHII between LEH and non-LEH conditions is calculated using Equation (5):

$$\Delta \text{SUHII}_{\text{LEH}} = \text{SUHII}_{\text{LEH}} - \text{SUHII}_{\text{non-LEH}} \quad (5)$$

Where  $\text{SUHII}_{\text{LEH}}$  is the SUHII under LEH conditions,  $\text{SUHII}_{\text{non-LEH}}$  is the SUHII under non-LEH conditions.

Following the studies of Chew et al. (2021), Jiang et al. (2019), and Chen et al. (2021), urban areas are defined according to the International Geosphere-Biosphere Programme (IGBP) definition of “Urban and Built-up Lands,” which refers to areas with “at least 30% impervious surface area, including building materials, asphalt, and vehicles”. And rural areas are defined as outside urban areas with at least 65% vegetation cover. Accordingly, in the context of Singapore, we identified urban areas as 1 km grids with the built-up percentage exceeding 30%, and rural areas as areas with tree cover greater than 80%.

#### *2.4. Feature engineering*

To identify the driving factors of SUHII responses to LEH, we considered urban indicators, including building morphology, natural environment, land use, socioeconomic factors, and LEH metrics. The spatial unit of calculating urban indicators is 1 km.

##### *2.4.1. LEH metrics*

We derive seven metrics to quantify frequency, intensity, and duration of LEH condition (Wang et al., 2022; Russo and Domeisen, 2023). These metrics include average

temperature (AVT), average intensity (HWI), average anomalies (AVA) of LEH condition, total number of LEH condition occurrences (HWN), sum of all participating LEH days (HWF), average LEH condition duration (AHD), and cumulative LEH (HEATcum) (Table 1).

Table 1: Summary of type, short name, full name, definition, and unit of LEH metrics.

Type	Short name	Full name	Definition	Unit
Intensity	AVT	Average Temperature of LEH	Average daily max temp. calculated over LEH days	°C
Intensity	HWI	Average Intensity of LEH	Sum of the differences between the daily max temp. and the daily 90 <sup>th</sup> percentile max temp. on LEH days, divided by the number of LEH conditions	°C
Intensity	AVA	Average Anomalies of LEH days	Average of the differences between daily max temp. and the daily 90 <sup>th</sup> percentile max temp. for LEH days	°C
Intensity	HEATcum	Cumulative LEH	Sum of the max temp. anomalies exceeding the 90 <sup>th</sup> percentile threshold (Tr90d) over LEH days	°C
Frequency	HWN	Total Number of LEH conditions	Total number of LEH conditions	Events
Frequency	HWF	Sum of LEH Days	Total number of LEH days	Days
Duration	AHD	Average LEH Condition Duration	Average duration of LEH conditions	Days

#### 2.4.2. Building morphology parameters

According to previous studies (Zheng et al., 2018; Li et al., 2021; Xi et al., 2023; Joshi et al., 2022; Biljecki and Chow, 2022), various urban morphology parameters were taken into account, as shown in Table 2. A showcase area of building morphology parameters at 1 km grid cells in the southern region of Singapore is shown in Fig. S1 in Appendix A.

Table 2: Summary of building morphology indicators calculated in the study.

Metrics (Abbreviation)	Expression	Definition	Unit
Building height (BH)	$BH = \frac{\sum_{i=1}^n H_i}{n}$ where $H_i$ = height of the building $i$ ; $n$ = number of the buildings in a grid cell	Average of building height	m <a href="#">(Zheng et al., 2018)</a>
Building surface fraction (BSF)	$BSF = \frac{A_{building}}{A_{grid}}$ where $A_{building}$ = total areas covered by buildings; $A_{grid}$ = the area of the grid cell	Fraction of total area covered by buildings within a grid cell	- <a href="#">(Zheng et al., 2018)</a>
Sky view factor (SVF)	The SVF is calculated by the SVF calculation tool in SAGA GIS with input data of building height and Digital Elevation Model (DEM)	Ratio of the visible sky area of a point in space to the total sky area	-
Building width (BW)	$BW = \frac{\text{build\_fraction} \times \text{Res}}{\text{build\_count}}$ where $\text{Res}$ = Resolution of a grid cell	Mean of building width within a grid cell	m
Street width (SW)	$SW = \frac{\text{Res}}{\text{build\_nrow}} - BW$ where $\text{build\_nrow} = \sqrt{\text{build\_fraction}} \times \frac{\text{Res}}{BW}$ , which assumes that buildings are square-shaped and evenly distributed in each grid cell	Mean of street width of each grid cell	m <a href="#">(Li et al., 2021)</a>
Street length (SL)	$SL = \sum_{i=1}^n L_i$ where $L_i$ = length of the street $i$ ; $n$ = number of streets in a grid cell	Sum of street length within a grid cell	m
Aspect ratio/height width ratio (H/W)	$H/W = \frac{BH}{SW}$	Ratio of height to width of a street canyon	-
Frontal area index (FAI)	$FAI(\theta) = \frac{A_\theta}{A_{plane}}$ where $\theta$ is the wind direction angle; $FAI(\theta)$ is the projected area of buildings in a specific wind direction; $A_{plane}$ is the calculation unit area. Here, we only calculate the FAI for northerly/easterly winds for the inter-city comparison to highlight the influence of buildings; $\theta$ is calculated as the product of the buildheight, buildnrow, and buildnrow in each grid cell. The grid cell area, namely the square of grid cell resolution, is taken as $A_{plane}$	Frontal area per unit height increment	- <a href="#">(Li et al., 2021; Joshi et al., 2022)</a>
The volume of the urban canopy (UCLV)	$UCLV = \max(h_i) \times A_{buffer}$ where $h_i$ is the height of the buildings in the buffer block; $A_{buffer}$ is the area of the buffer zone. To create the buffer zone to include the street, we use half of the street_width of each grid cell as the buffer zone for each grid cell	Volume of the urban canopy	- <a href="#">(Joshi et al., 2022)</a>

*Continued on next page*

Table 2: (continued)

Metrics (Abbreviation)	Expression	Definition	Unit
Porosity (Po)	$P_o = \frac{(\text{UCLV} - \text{BV})}{\text{UCLV}}$ where $\text{BV} = \sum_{i=1}^n A_i \times h_i$ ; $A_i$ is the area of the building located in the buffer zone of the grid cell	Ratio of the empty volume in an urban canopy to the volume of the urban canopy (Joshi et al., 2022)	-
Average distance between the adjacent buildings (DB)	$D_{\min} = \frac{1}{n} \sum_{i=1}^n \min_{1 \leq j \leq n-1} (D_{ij})$ where $D_{ij}$ is the distance between one building and the rest of the buildings; $n$ is the number of buildings in the grid	Average distance between adjacent buildings in a grid cell, representing the compactness or sprawl of buildings within the grid cell (Joshi et al., 2022)	m
Average distance between the center of the grid cell and buildings (DC)	$DC = \frac{\sum_{i=1}^n D_{c(i)}}{n}$ $DC\_i$ is the distance from the grid cell's center to the building's center; $n$ is the number of buildings in the grid cell	Average distance of all building centers from the center of the grid cell (Joshi et al., 2022)	m
Open space ratio (OSR)	$OSR = \frac{1-GSI}{GSI}$ where $GSI = \frac{\sum_{i=1}^n A_{bu(i)}}{A_{bl}}$ ; $A_{bu}$ is the area occupied by the building in the grid cell; $A_{bl}$ is the area of the grid cell; $n$ is the number of buildings in the grid cell	Ratio of open areas to the built area, describing the intensity of use of non-built ground (Joshi et al., 2022)	%
Height of roughness elements (HRE)	$HRE = \frac{\sum_{i=1}^n A_{bu(i)} \times h_{bu(i)}}{A_{buffer}}$ where $A_{bu}$ is the area occupied by the building in the grid cell; $h_{bu}$ is the height of the building within the buffer zone of the grid cell; $A_{buffer}$ is the area of the buffer zone; $n$ is the number of buildings within the grid cell	Average building height in the urban canopy (Joshi et al., 2022)	m

#### 2.4.3. Land use indices

With reference to Singapore's master plan, we divided land use indices into six categories, including natural spaces, infrastructure, commercial, industrial, residential, and special use (see Table. 3).

Table 3: Category of land use types

Category	Types
Natural Spaces	Open space, Water body, Park, Beach area, Agriculture
Infrastructure	Road, Utility, Transport facilities, Mass rapid transit, Light rapid transit, Port airport
Commercial	Commercial institution, Commercial, Business park, White, Business park white
Industrial	Business 2, Business 1, Business 2 white, Business 1 white
Residential	Residential institution, Residential, Commercial Residential, Residential with commercial
Special use	Sports recreation, Reserve site, Special use, Hotel

#### 2.4.4. Natural environmental indices

The natural environmental indices considered in this study, including vegetative indices, water index, etc., are shown in Table 4. A showcase area of natural environmental indices at 1 km grid cells in the southern region of Singapore is presented in Fig. S2 in Appendix A.

Table 4: Summary of natural environmental indices used in the study.

Short name	Full name	Definition
NDVI	Normalized Difference Vegetation Index	NDVI is defined as the quotient of the difference between the reflectivity of the near-infrared (NIR) and the visible red light channel (RED), calculated as (Sun et al., 2021): $NDVI = \frac{NIR - RED}{NIR + RED}$
EVI	Enhanced Vegetation Index	EVI is the most common alternative vegetation index that addresses soil and atmosphere limitations with NDVI (Liu and Huete, 1995; Xue and Su, 2017). The EVI2 index can be used to produce an EVI-like vegetation index (Jiang et al., 2008), calculated as: $EVI2 = 2.5 \times \frac{(NIR - RED)}{NIR + (2.4 \times RED) + 1}$
MSAVI2	Modified Soil-Adjusted Vegetation Index	MSAVI2 is a good index for areas that are not completely covered with vegetation and have exposed soil surface (Xue and Su, 2017), which is calculated as: $MSAVI2 = \frac{(2 \times NIR + 1) - \sqrt{(2 \times NIR + 1)^2 - 8 \times (NIR - RED)}}{2}$
SAVI	Soil Adjusted Vegetation Index	SAVI is a modification of the NDVI with a correction factor $L$ for soil brightness, which is calculated as: $SAVI = \frac{(NIR - RED)}{(NIR + RED + L)} \times (1 + L)$ where the value of $L$ is 0.5, which is the default value and works well in most situations.

*Continued on next page*

Table 4: (continued)

Short name	Full name	Definition
AVI	Advanced Vegetation Index	AVI is the advanced vegetation index, which reacts more sensitively to vegetation quantity and is able to highlight subtle differences in canopy density (Rikimaru et al., 2002). It is calculated as:
		$AVI = \sqrt[3]{((NIR + 1) \times (256 - RED) \times (NIR - RED))}$
SI	Shadow Index	SI is the shadow index, which increases as the forest density increases, and this shadow pattern affects the spectral responses (Rikimaru et al., 2002). SI is calculated as:
		$SI = \sqrt[3]{(256 - BLUE) \times (256 - GREEN) \times (256 - RED)}$ where BLUE is the visible blue light channel, and GREEN is the visible green light channel.
BI	Bare Soil Index	BI is the bare soil index, which enhances the identification of bare soil areas and fallow lands (Mzid et al., 2021). BI is calculated as:
		$BI = \frac{(SWIR1 + RED) - (NIR + BLUE)}{(SWIR1 + RED) + (NIR + BLUE)}$ where SWIR1 is the shortwave infrared 1 band processed to orthorectified surface reflectance.
ISF	Impervious surface area fraction	ISF is defined as the area of impervious surface divided by the area of the grid cell. The impervious surface area data is obtained from the Global Artificial Impervious Area (GAIA) data (Version 2022) dataset.
NDWI	Normalized Difference Water Index	NDWI is developed to characterize surface water cover and to allow for the measurement of surface water extent (McFeeters, 2013), and calculated as follows:
		$NDWI = \frac{(GREEN - NIR)}{(GREEN + NIR)}$

#### 2.4.5. Socioeconomic indicators

We also considered socioeconomic indicators, including population density (PopD) and the night-time light (NTL) index. The population density at 1 km spatial resolution was obtained from the open-access WorldPop dataset. WorldPop is a high-resolution population dataset that has been used for disaster management and environmental impact

assessment (Zhu et al., 2020). The NTL data were obtained from the global 500-meter resolution "NPP-VIRS-like" dataset (Chen et al., 2020) (National Earth System Science Data Center, National Science & Technology Infrastructure of China). Then, we processed the night light index to the 1 km spatial resolution.

#### 2.4.6. Multicollinearity test

To ensure the explanatory variables were not affected by multicollinearity, we assessed multicollinearity using the variance inflation factor (VIF) and applied a threshold of 10 (Yang et al., 2024; Benito, 2021a). Variables with VIF values greater than 10 were excluded from further analysis. Only non-multicollinear variables that passed this test were retained for model development. Table 5 presents the set of explanatory variables used in the ML model.

Table 5: Dependent variables

Type of indicators	Definition	VIF
<b>2D Buildings</b>		
BW	Average building width	1.98
SW	Street width	6.76
SL	Street length	2.29
BH	Average building height	5.93
OSR	Open space ratio	6.86
DB	Average distance between adjacent buildings in a grid cell	3.18
DC	Average distance from the centroid to buildings in a grid cell	2.93
<b>3D Buildings</b>		
H/W	Building height to street width ratio	4.26
Po	Porosity	3.78
GPR	Gross plot ratio	3.04
<b>Vegetation and water indices</b>		
AVI	Advanced Vegetation Index	9.68
SI	Shadow Index	6.90
NDWI	Normalized Difference Water Index	6.66
<b>Land use types</b>		
PctTrees	Percentage of trees area	5.24
PctCI	Percentage of Masterplan area covered by commercial and industrial	2.76
PctInfra	Percentage of Masterplan area covered by infrastructure	2.41
PctSpecUse	Percentage of Masterplan area covered by special use	2.12
PctRes	Percentage of Masterplan area covered by residential	3.89
<b>Social-economic indices</b>		
PD	Estimated population density in a grid cell	2.04
NL	Average night light values in a grid cell	3.91
<b>LEH metrics</b>		
AVT	Average temperature of LEH	5.05
HWN	Total number of LEH conditions	1.23
HWI	Average intensity of LEH	2.37

## 2.5. Global and local feature importance exploration

### 2.5.1. SpatialRF model construction

To justify the use of the spatial machine learning (ML) model in explaining SUHII responses to LEH, it is important to examine the spatial autocorrelation of the training data across different distance thresholds.

We evaluated the spatial autocorrelation of the explanatory and predictor variables at different distance thresholds in Singapore. The result shows that the spatial autocorrelation of the explanatory and predictor variables was strong, especially in the range of 2 km to 4 km (see Fig. S3 in Appendix B), which highlights that the SpatialRF model is the appropriate way to take into account the spatial autocorrelation of the model residuals.

Subsequently, we used the SpatialRF to model SUHII responses to LEH. The advantage of the SpatialRF is minimizing the spatial autocorrelation of the model residuals by understanding the spatial structure and generating spatial predictors (Benito, 2021b). The spatial predictors are generated from the distance matrix of the data points, which are obtained by extracting the latitude and longitude of the centroid of each grid. In addition, as we build the model for explanatory rather than predictive purposes, all available samples are utilized for model training.

Furthermore, model performance was evaluated using R-squared and Root Mean Squared Error (RMSE) metrics, derived from predictions on out-of-bag data, which is the fraction of data not used for training individual trees (Benito, 2021b). Variable importance was assessed by measuring the increase in mean error on the out-of-bag data when a predictor is permuted (Benito, 2021b). Additionally, response curves were analyzed to explore how dependent variables respond to changes in explanatory variables.

### 2.5.2. Using Shapley Additive exPlanations in Explainable Machine Learning

To investigate the dominant drivers of SUHII responses to LEH in local areas, the SHAP model was employed to quantify and explain the contribution of individual predictors to the dependent variable. The Shapley value, derived from game theory, provides a fair allocation of the effect of each predictor in the model (Li, 2022; Yang et al., 2024). The formula for calculating the Shapley value is as follows (Štrumbelj and Kononenko,

[2014]):

$$\phi_i(x) = \sum_{Q \subseteq S \setminus \{i\}} \frac{|Q|!(|S| - |Q| - 1)!}{|S|!} (\Delta_{Q \cup \{i\}}(x) - \Delta_Q(x)). \quad (6)$$

where  $\phi_i(x)$  is the Shapley value that reflects the contribution of the variable  $i$ ,  $S$  denotes the set with the number of variables  $i$ ,  $\Delta_{Q \cup \{i\}}(x)$  and  $\Delta_Q(x)$  represents the model results with or without the variable  $i$ , respectively. In this study, the SHAP model is applied to interpret the SpatialRF (Molnar and Schratz, 2020). By computing Shapley values, we can efficiently determine the contributions of individual features for each prediction. This approach allows us to uncover the nonlinear effects within the model by providing localized explanations of the relationships between predictors and the SUHII variations.

#### 2.5.3. Clustering process of local importance of features

To identify local areas having similar local feature importance of SUHII responses to LEH, we applied the clustering method to the local SHAP value of indicators. First, we categorized the indicators into five main groups: building morphology, vegetation, water, land use, LEH, and socio-economic indicators. To reduce dimensionality and identify key contributing indicators, we performed principal component analysis (PCA) on the local SHAP values for these categories. Clustering was then conducted based on the first principal component extracted for each of the five categories. When the number of clusters is unknown, unsupervised classification methods can help reveal similar groups. In this study, we employed the Agglomerative Hierarchical Clustering (AHC) algorithm, which is widely used across various fields (Tang et al., 2019). AHC begins with each data point as an individual cluster and iteratively merges the closest pairs based on similarity, ultimately producing a hierarchical tree structure (Zhou et al., 2016; Ip et al., 2010). The similarity between objects is quantified using Euclidean distance, and Ward's linkage method is used to combine clusters in a way that minimizes the variance within each cluster (Govender and Sivakumar, 2020). The output of the AHC algorithm is a dendrogram, which helps in selecting the optimal number of clusters.

### 3. Results

#### 3.1. SUHII responses to LEH and dominant drivers for Singapore

The extreme heat showed spatial heterogeneity within the city, and different areas exhibited different characteristics of extreme heat. The spatial patterns of various LEH metrics, including AVT (average temperature of LEH), HWI (average intensity of LEH), and HWN (total number of LEH conditions), are presented in Fig. 3. In particular, the spatial pattern of AVT and HWI shows they had a similar representation. The northeast, southeast, and industrial areas exhibited the highest AVT, around  $34.3^{\circ}\text{C}$ , and also experienced pronounced extreme temperature anomalies in Geylang and Tampines. Other areas of the south and central regions, including Queenstown and Clementi, had the lowest temperature of extreme heat and the lowest extreme temperature anomalies. By contrast, HWN displayed a different spatial pattern from AVT and HWI. The highest number of LEH occurrences was concentrated in the northeastern regions (e.g., Pasir Ris and Sengkang) and the western areas of Jurong West. Overall, extreme heat showed intra-urban variation in high temperatures, underscoring the importance of considering local-scale extremes.

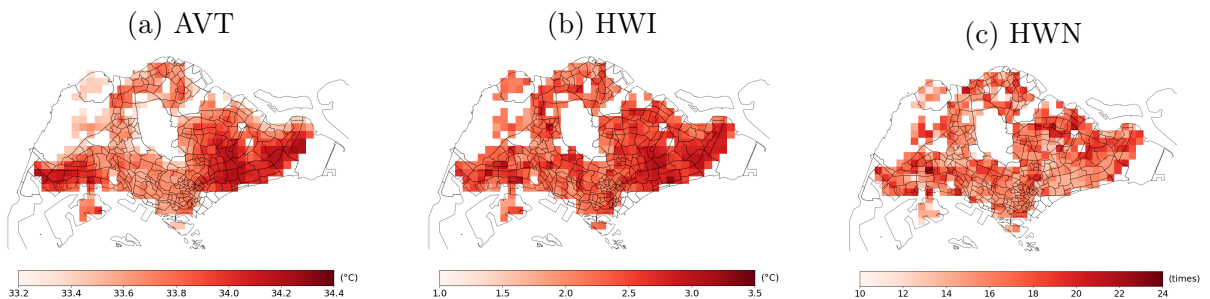


Figure 3: Spatial distribution of LEH metrics for (a) AVT, (b) HWI, and (c) HWN.

The spatial pattern of daytime and nighttime SUHII responses to LEH is displayed in Fig. 4. Daytime and nighttime SUHII were amplified by LEH in most areas, while their spatial distributions and intensities of SUHII variations differed. Specifically, during the daytime, the maximum increased SUHII reached approximately  $3.2^{\circ}\text{C}$ , particularly in the northeastern and eastern regions, including Ang Mo Kio, Hougang, and Tampines.

In contrast, nighttime SUHII responses to LEH were less pronounced, with the maximum increase of around  $0.6^{\circ}\text{C}$ , mainly observed in the western and central regions such as Jurong West, Jurong East, Clementi, Queenstown, and Bukit Merah. These results demonstrate that LEH had a greater amplifying effect on daytime SUHII than on nighttime and revealed distinct spatial patterns between day and night.

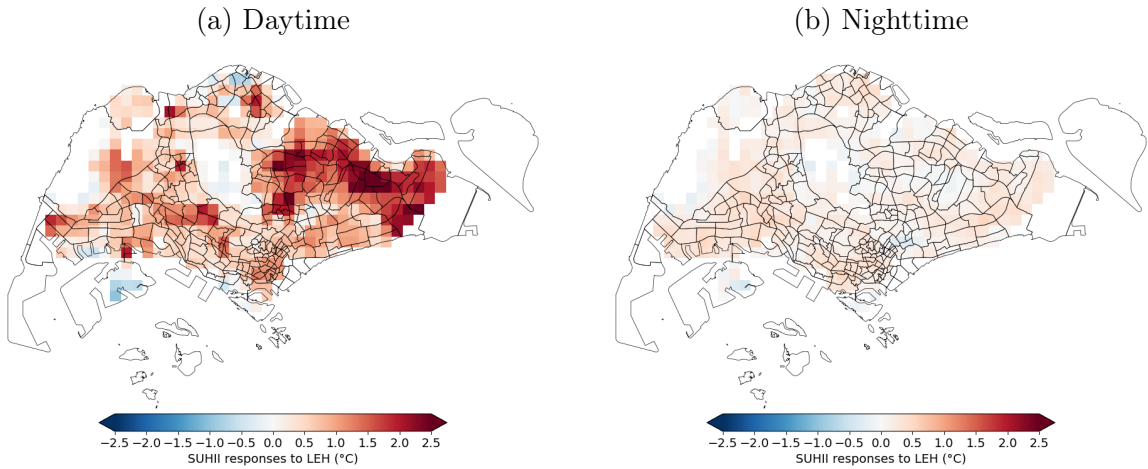


Figure 4: Spatial pattern of (a) daytime and (b) nighttime SUHII responses to LEH.

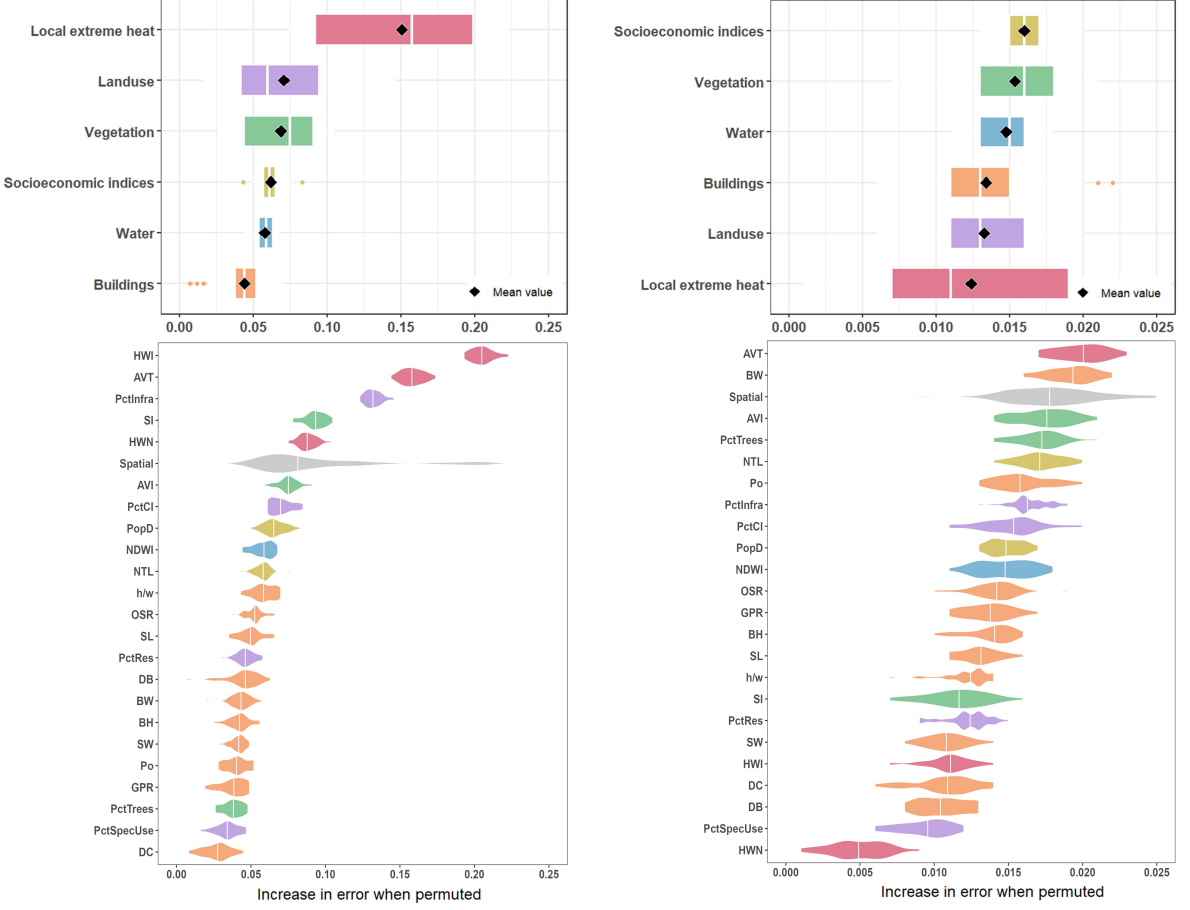
The SUHII changes may be associated with local climate, urban layout, land use, and anthropogenic heat. To understand the drivers of SUHII responses to LEH, the spatialRF model was applied, using SUHII responses to LEH as the predictable variable and non-multicollinear factors as explanatory variables. The results of model performance show that the model of daytime SUHII responses to LEH achieved R-square values exceeding 63%, while the nighttime model achieved R-square values exceeding 45% (Table 6). We further tested whether adding water area percentage, mean HDB resale prices, POIs, and transport points could improve performance. Data were sourced from OpenStreetMap and the Singapore Open Data portal. The results in Tables S1 and S2 in the Appendix C show that these features did not enhance predictive accuracy; in some cases, performance declined. These align with previous literature indicating that geographic factors account for about 40% of the variation in urban heat (Bian, 2025). A substantial portion of the variation remains unexplained, mainly because urban heat is highly sensitive to dynamic factors such as wind, cloud cover, and anthropogenic heat. It is suggested that our models

can provide reasonable explanations of the role of geographical features for daytime and nighttime SUHII responses to LEH.

Table 6: Model performance of daytime and nighttime SUHII responses to LEH.

Models	Model performance (median +/- mad)	
	R-square (oob)	Normalized RMSE
Daytime SUHII variations	0.639 +/- 0.0036	0.194 +/- 0.0010
Nighttime SUHII variations	0.451 +/- 0.0053	0.232 +/- 0.0015

The importance scores of factors driving daytime and nighttime SUHII responses to LEH across the entire city are shown in Fig. 5, revealing the dominant contributors during both periods. Local extreme heat, vegetation, and land use were identified as the primary drivers of daytime SUHII variations, whereas nighttime variations were mainly influenced by socioeconomic factors, vegetation, and water. Specifically, the average intensity of LEH (HWI) was the key factor of the local extreme heat feature category during the daytime, while nighttime light (NTL) of the socioeconomic feature category played a dominant role at night. These findings highlight that the dominant features governing daytime and nighttime SUHII responses are different.



(a) Daytime importance scores for feature categories and factors (b) Nighttime importance scores for feature categories and factors

Figure 5: The importance scores of different feature categories and various factors for (a) daytime and (b) nighttime SUHII responses to LEH.

### 3.2. Dominant factors of SUHII responses to LEH at local areas in Singapore

We used the SHAP model to interpret the spatialRF model, with the SHAP values of factors in local areas representing the local importance of each feature. Based on these local SHAP values, the clustering approach was applied to group the dominant drivers. The analysis identified feature clusters for both daytime and nighttime SUHII responses to LEH, as shown in Fig. S4 in Appendix D. The spatial distributions of three clusters of local feature importance are presented in Fig. 6a and Fig. 6b, for daytime and nighttime, respectively.

Cluster I is characterized by the lowest SUHII variations under LEH during the daytime. Building morphology and LEH negatively contribute to SUHII increases, with standardized SHAP values of -0.6 and -0.7, suggesting that shading effects from built form

and ventilation reduced daytime warming, while water slightly positively contributed to SUHII increases. At night, the lowest SUHII changes were mainly due to the result that building morphology and socio-economic factors became important negative contributors, with standardized SHAP values of -0.9 and -1.1, and water continuously played a positive role. The cluster I was only distributed in small local areas, while most areas are characterized by cluster II. The cluster II exhibited SHAP values of most factors close to zero for both daytime and nighttime, implying a more balanced influence of multiple factors on SUHII changes. These areas may represent thermally neutral zones within the city.

Cluster III, associated with the highest SUHII increases, was mainly distributed in the northeast, including Yio Chu Kang and Serangoon, the east, including Paya Lebar, Bedok, and Tampines, and the areas of Bukit Timah during the daytime. At night, the highest SUHII increases were mainly concentrated in the industrial areas of Pioneer and Tuas, Jurong West in the western region, Queenstown in the south region, as well as Tampines in the east. Daytime responses are primarily driven by socio-economic and LEH, with standardized SHAP values of 0.5 and 0.7, reflecting the amplification of local warming by intensive daytime human activities and extreme heat. At night, socio-economic and vegetation factors become the leading positive drivers, likely because of higher nighttime activity levels and thermal storage effects in vegetation. These patterns indicate that socio-economic factors consistently serve as dominant drivers within Cluster III.

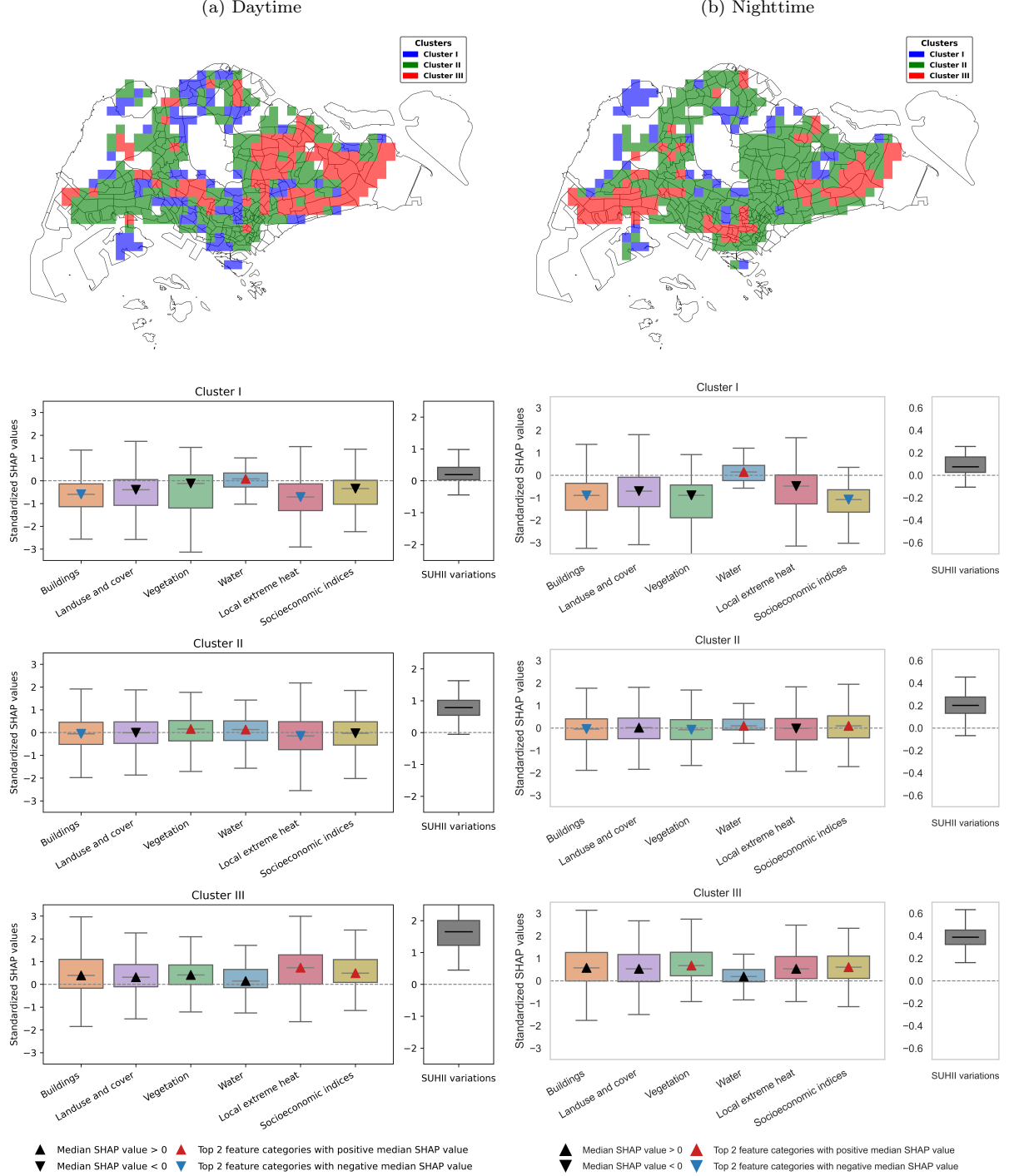


Figure 6: Spatial clusters and boxplots illustrating the drivers of SUHII responses to LEH during (a) daytime and (b) nighttime. Bottom panels display standardized SHAP values of six grouped feature categories across three clusters. Each boxplot shows the median SHAP value (▲ upward for positive, ▼ downward for negative), and the top 2 feature categories with positive (▲ red) and negative (▼ blue) median SHAP values in each cluster.

### 3.3. Nonlinear associations for hotspots of SUHII responses to LEH

The day–night clusters of dominant drivers of SUHII responses to LEH are shown in Fig. 7. Hotspot areas with the highest increases in SUHII are highlighted, corresponding to clusters II–III (orange), III–II (blue), and III–III (purple), indicating that these areas are experiencing overheating in SUHII increases.

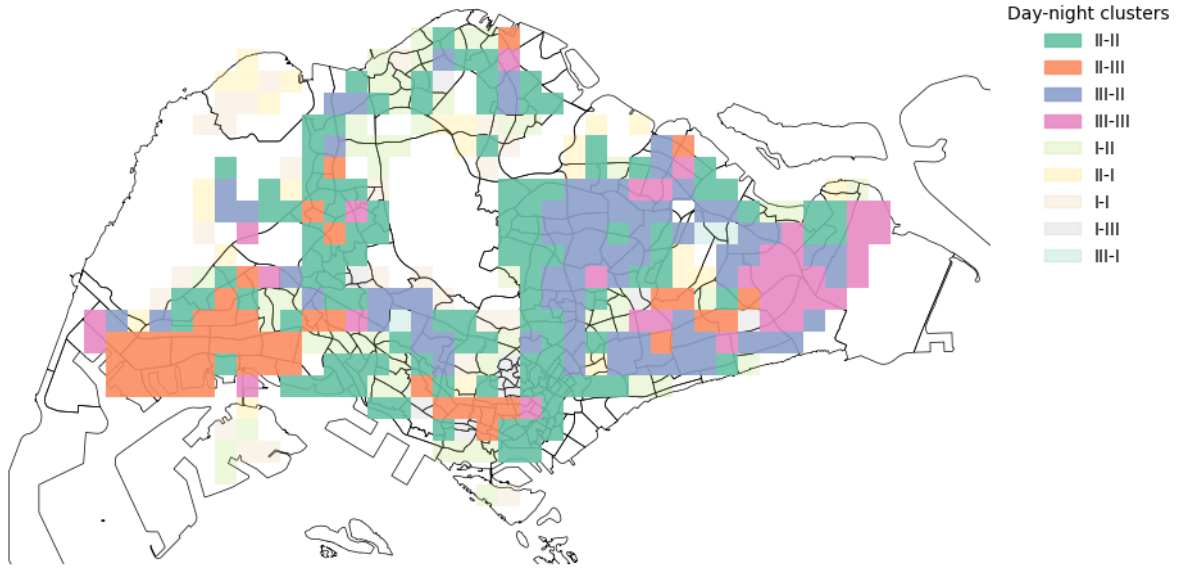


Figure 7: Day-night clusters of dominant local drivers of SUHII responses to LEH.

Furthermore, the nonlinear associations between influencing factors and SUHII responses in hotspot areas are illustrated in Fig. 8. In areas of type II–III, height-to-width (H/W) ratios between 2.5 and 7.5 exhibited negative effects on SUHII for both day and night. For areas of type III–II, the SI exhibits a slightly inverted U-shaped relationship. When SI exceeded 255.88, the positive SHAP effect value declined, and the slope plateaued. As for the percentage of trees, the SHAP effect remained consistently positive, suggesting that increasing tree coverage had a limited effect on reducing SUHII. In addition, when Po exceeded 0.4, its SHAP effect value stabilized, indicating that further increases in Po led to little change in its contribution. Moreover, the SHAP value of NDWI displayed a distinct U-shaped pattern, initially increasing and then decreasing. It peaked at  $-0.45$ , representing the point of greatest positive contribution to SUHII. Beyond this value, the SHAP effect declined, implying that additional water presence helps mitigate SUHII during both daytime and nighttime. Similarly, in other types of areas,

higher NDWI values were associated with a decrease in SUHII.

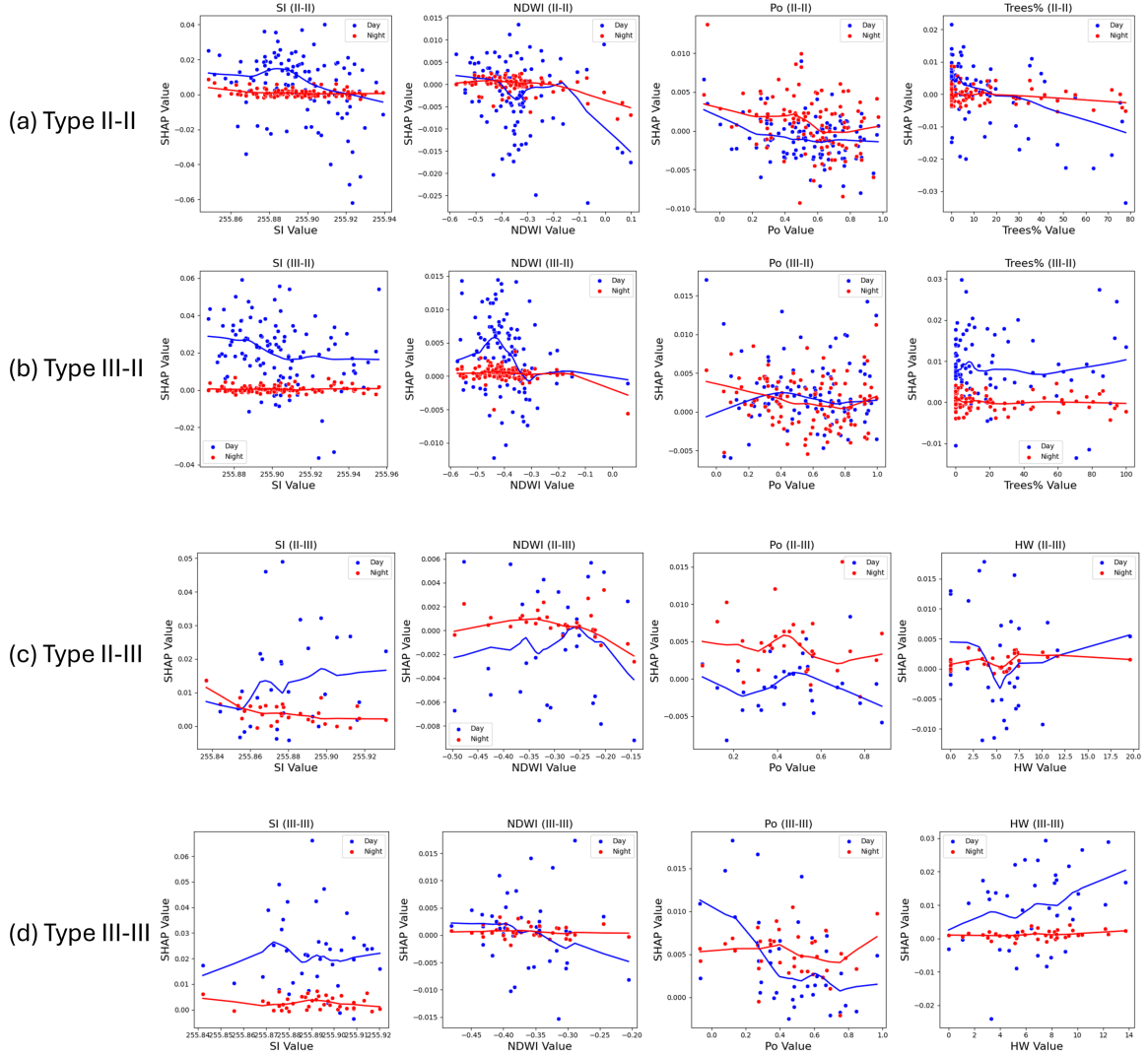


Figure 8: SHAP dependence plots illustrating day–night cluster of SUHII responses to LEH for (a) II–II, (b) III–II, (c) II–III, and (d) III–III.

## 4. Discussion

### 4.1. Uncovering the extreme heat characteristics at local scales

In the context of global climate change, cities are increasingly experiencing extreme heat events (Perkins-Kirkpatrick and Lewis, 2020; Perkins-Kirkpatrick and Gibson, 2017; Qiu and Yan, 2020). Combined with the UHI effect, urban areas are facing more frequent and intensified overheating (Tan et al., 2010; Basara et al., 2010). Previous studies have typically defined extreme heat days at the city-wide scale (Wei et al., 2021; Founda and Santamouris, 2017), while such approaches overlook the local variations in extreme

temperature within a city. To consider this, our study introduced the concept of LEH and examined its spatial patterns and characteristics in Singapore. We found that different areas exhibited distinct LEH characteristics, including average temperature, intensity, and frequency. Notably, the highest frequency of LEH occurrence was observed in the northeastern part of the city, consistent with the findings of Yu et al. (2023), which were based on weather station data in Singapore. Beyond this, we identified that the highest intensity and temperature of LEH occurred in the southeastern region, indicating that local temperatures in this region were not only higher but also had more changes than in other areas.

#### *4.2. Localized synergies between SUHIs and extreme heat and its underlying drivers*

UHI is typically a localized phenomenon driven by microclimate and urban features. The UHII can be exacerbated by extreme heat at the local scale; however, the spatial patterns and underlying drivers of this interaction are not fully understood. To address this gap, we employed an interpretable spatial ML method to identify the dominant local drivers of the interaction between SUHI and extreme heat. The spatialRF model was used due to its advantages in analyzing spatially continuous phenomena compared to conventional ML approaches such as Random Forest and XGBoost (Yang et al., 2022; He et al., 2024). Furthermore, the SHAP model was innovatively applied to explain the spatialRF model, extending its typical use beyond traditional ML models and providing a more reasonable interpretation. Building on the use of an interpretable spatialRF model, a clustering approach was applied to the SHAP values of local features to identify the number of groups of local drivers and uncover their spatial patterns.

In our study, we found that local synergies between SUHIs and extreme heat manifest differently during daytime and nighttime in Singapore. The daytime SUHII increases reached approximately 3 °C, while the maximum nighttime SUHII increase was around 0.6 °C. This observation aligns with findings from most city-scale studies, which have reported that UHIs are more intense during the daytime than at night under extreme heat conditions, such as in cities of Korea (Kim and Baik, 2004) and Shanghai, China (Tan et al., 2010). The daytime SUHII increases are mostly related to LEH and land use,

whereas the nighttime SUHII increases are more closely associated with socioeconomic factors, suggesting that greater anthropogenic heat plays a significant role, which aligns with previous findings from Beijing at the city scale (He et al., 2020).

At the local scale, different areas exhibit distinct dominant drivers and are associated with different levels of SUHII variation. The most pronounced daytime SUHII increases are observed in the northeastern areas, which are primarily composed of LCZ 4 (open high-rise) (Luo et al., 2023). These increases are mainly driven by socioeconomic factors and local extreme temperatures. This finding is consistent with previous studies conducted in Beijing (Zong et al., 2021) and Guangzhou (Luo et al., 2023), suggesting that open high-rise building forms generally provide good ventilation conditions and therefore do not predominantly drive SUHII increases. The most intense nighttime SUHII increases occur in the southwestern industrial areas and in the eastern parts of the city, where they are positively associated with LEH and socioeconomic factors. This indicates that socioeconomic influences are consistently dominant in driving SUHII increases, particularly during nighttime, likely due to continuous anthropogenic heat emissions from industrial and transportation activities.

#### *4.3. Potential strategies for mitigating SUHII increases under local extreme heat conditions*

As for mitigation strategies to decrease SUHII under LEH conditions, we examined the nonlinear association between features and SUHII. For the areas with high SUHII increases, the nonlinear association results show that more vegetation had a limited reducing contribution to SUHII both during the daytime and nighttime. This suggests the cooling potential of greens tends to achieve saturation in cities with hot and humid climates, which aligns with the previous study by Rogers et al. (2019). However, we found that water bodies demonstrated significant cooling potential for daytime and nighttime SUHII under extreme heat conditions. Also, water management has been shown to be the cooling solution for mitigating urban heat in other cities, such as Shanghai in China and Karlsruhe and Berlin in Germany (Du and Zhou, 2022; Walther and Olonscheck, 2016). Our findings emphasize that for climate-resilient urban planning, measures to mitigate

daytime and nighttime SUHII under extreme heat conditions in local areas should go beyond planting more greenery. Introducing or expanding urban water or implementing water-spraying interventions can be considered an urban cooling practice.

#### *4.4. Limitations and future opportunities*

This study comprehensively explored the spatial pattern of local extreme heat and its impacts on SUHII and examined the key drivers of SUHII responses to LEH by considering factors related to the environment, building morphology, socioeconomic characteristics, and local extreme heat. While some limitations exist, future studies should consider the following points. Our spatial RF model explained approximately 63% of the daytime SUHII variations and 45% of the nighttime SUHII variations, primarily relying on geographical features. A substantial portion of the unexplained variation is sensitive to dynamic factors such as wind, cloud cover, and anthropogenic heat (Bian, 2025), suggesting that future studies should incorporate additional variables. For instance, meteorological factors such as wind speed, wind direction, and relative humidity may influence the interactions between UHI and extreme heat. In addition, our study focused on the impact of local extreme heat on SUHII. Future research could, in turn, explore the influence of SUHII on local extreme heat occurrences and characteristics.

## **5. Conclusion**

Our study investigated the spatial pattern of SUHII responses to LEH, addressing the gap in considering the extreme heat at the local scale and identifying the key drivers using an interpretable spatial RF model. We found that LEH increased SUHII in most urban areas during the daytime and nighttime. Daytime SUHII increases were higher than nighttime, around 3 °C and 0.6 °C, respectively. Besides, the spatial distribution of SUHII responses to LEH differed between day and night. The daytime SUHII increases were primarily concentrated in northeastern areas, while nighttime SUHII increases were prevalent in the western areas. To identify the dominant factors, we employed the spatialRF model. The spatialRF model achieved R-squared values exceeding 63% for predicting daytime SUHII responses to LEH and 45% for nighttime SUHII responses. During

the day, LEH, vegetation, and land use were the primary drivers of SUHII variation. At night, socioeconomic factors, vegetation, and water were the main contributors. Notably, the role of potential human activities became more significant during nighttime, suggesting a shift in dominant influencing factors from day to night. Furthermore, we identified three clusters of dominant drivers of SUHII variations for daytime and nighttime. For the hotspots of SUHII increases, socioeconomic factors consistently drove SUHII increases. Moreover, nonlinear associations between the factor value and its SHAP values in hotspots showed that the cooling effect of planting more trees reached saturation, and increasing the water body appeared to be a more effective way to mitigate the SUHII increase under LEH conditions.

## Data availability statement

The Global Daily near-surface air temperature dataset can be freely accessed at <https://gee-community-catalog.org/projects/airtemp/>. The MODIS Gap-filled Long-term Land Surface Temperature Daily dataset can be freely accessed at [https://gee-community-catalog.org/projects/daily\\_lst/](https://gee-community-catalog.org/projects/daily_lst/). The Landsat 5/7/8/9 images can be freely accessed at Google Earth Engine. The Sentinel-2 10m land use/land cover dataset can be freely accessed at <https://livingatlas.arcgis.com/landcoverexplorer/>. The Masterplan for 2019 in Singapore can be freely accessed at <https://beta.data.gov.sg/>. The nighttime light obtained from global 500-meter resolution "NPP-VIRS-like" datasets can be freely accessed at the National Earth System Science Data Center, National Science & Technology Infrastructure of China (<http://geodata.nnu.edu.cn/>). The road data can be freely accessed from OpenStreetMap. The Global Artificial Impervious Area (GAIA) data can be freely accessed at [https://www.x-mol.com/groups/li\\_xuecao/news/48145](https://www.x-mol.com/groups/li_xuecao/news/48145). The population density at 1 km resolution can be freely accessed at Worldpop (<https://hub.worldpop.org/geodata/listing?id=76>).

## **Acknowledgment**

The research was conducted partly at the Future Cities Lab Global at the Singapore-ETH Centre, established collaboratively between ETH Zurich and the National Research Foundation Singapore. This research is supported by the National Research Foundation Singapore (NRF) under its Campus for Research Excellence and Technological Enterprise (CREATE) programme. The first author additionally acknowledges support from the China Scholarship Council (202206040009) and DoA Graduate Studentship from the Department of Architecture at the National University of Singapore (NUS). We greatly appreciate the anonymous reviewers and the editor for their helpful comments and constructive suggestions that improved this work.

## **Declaration of Generative AI and AI-assisted Technologies in the Writing Process**

During the preparation of this work the authors used ChatGPT in order to proofread the text. After using this tool, the authors reviewed and edited the content as needed and take full responsibility for the published article.

## Appendix A. The showcase area of calculated building morphology and natural environmental indices

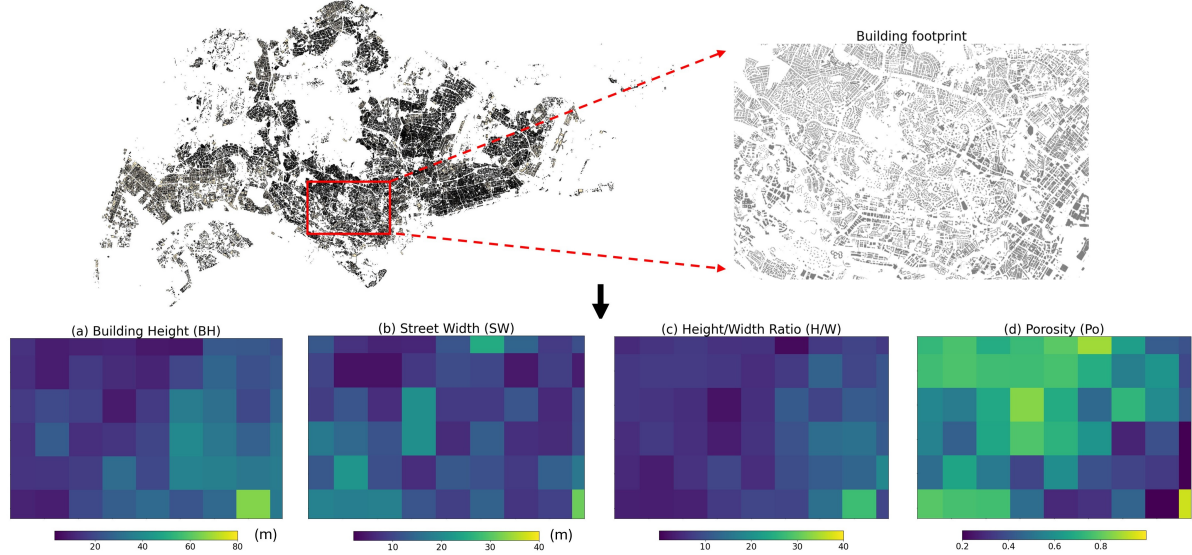


Figure S1: The showcase area of calculated (a) building height, (b) street width, (c) porosity, and (d) H/W at  $1 \times 1$  km grids along the southern region in Singapore. Data source: (c) OpenStreetMap contributors.

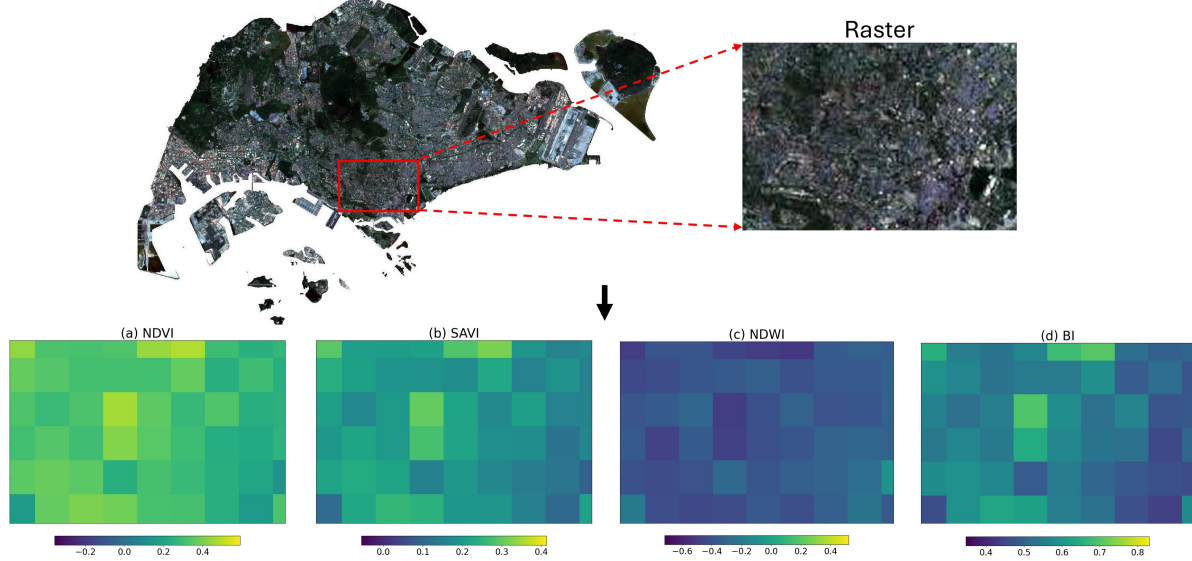


Figure S2: The showcase area of calculated (a) NDVI, (b) SAVI, (c) NDWI, and (d) BI at  $1 \times 1$  km grids along the southern region in Singapore. Data source: Landsat imagery.

## Appendix B. Spatial autocorrelation of the response variable and predictors across different distance thresholds

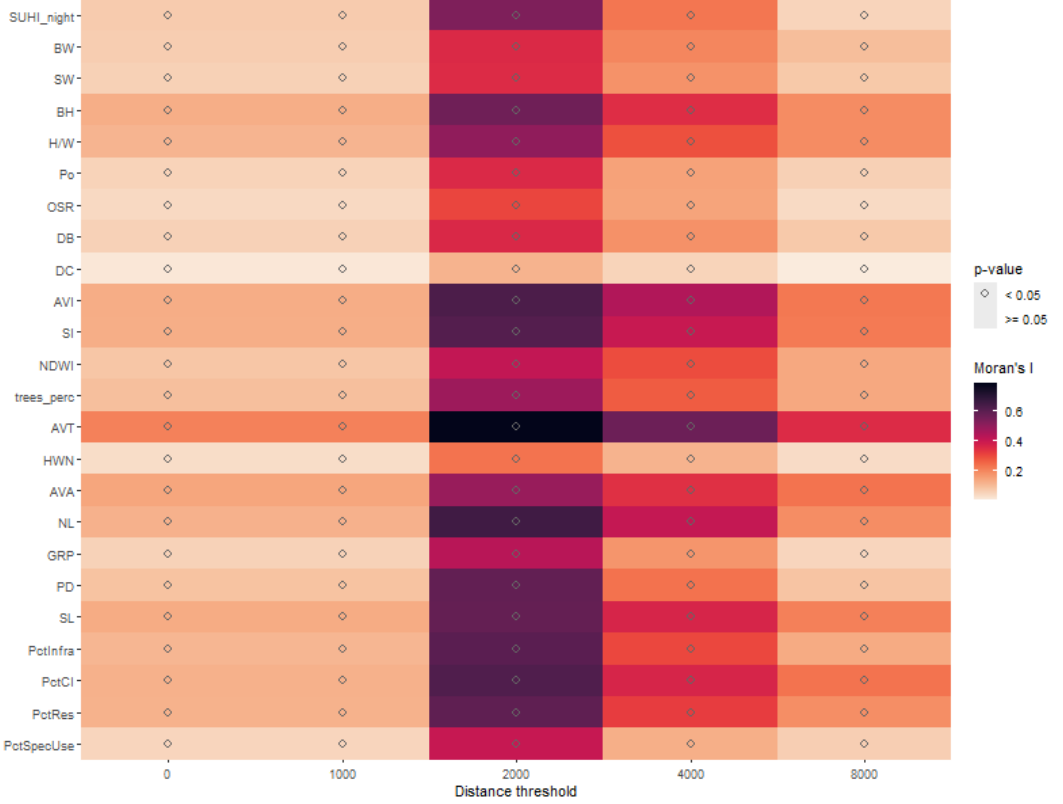


Figure S3: The spatial autocorrelation of the response variable and predictors across different distance thresholds. Low Moran's I and p-values equal to or larger than 0.05 indicate no spatial autocorrelation for the given variable and distance threshold.

## Appendix C. Model performance of experiments with incorporating additional features for daytime and nighttime SUHII responses to LEH

Table S1: Model performance of experiments with additional features for daytime SUHII responses to LEH.

Experiment (Day-time SUHII responses)	Count of POI	Count of transport points	Percentage of water area	HDB prices	R-square (oob)
Baseline					0.639 +/- 0.0036
1	✓	✓			0.638 +/- 0.0024
2	✓	✓	✓		0.631 +/- 0.0041
3	✓	✓	✓	✓	0.635 +/- 0.0043

Table S2: Model performance of experiments with additional features for nighttime SUHII responses to LEH.

Experiment (Nighttime SUHII responses)	Count of POI	Count of transport points	Percentage of water area	HDB prices	R-square (oob)
Baseline					0.451 +/- 0.0053
1	✓	✓			0.45 +/- 0.0041
2	✓	✓	✓		0.451 +/- 0.0041
3	✓	✓	✓	✓	0.449 +/- 0.0046

## Appendix D. Agglomerative hierarchical clustering dendrogram of daytime and nighttime SUHII responses to LEH

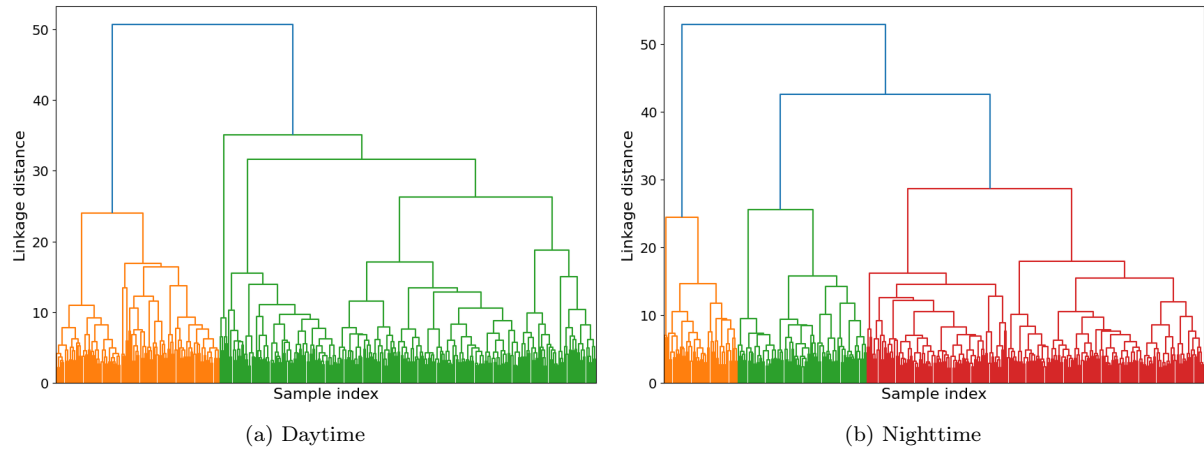


Figure S4: Agglomerative hierarchical clustering dendograms of (a) daytime and (b) nighttime SUHII responses to LEH.

## References

- Basara, J.B., Basara, H.G., Illston, B.G., Crawford, K.C., 2010. The impact of the urban heat island during an intense heat wave in oklahoma city. *Advances in Meteorology* 2010, 230365.
- Benito, B., 2021a. Blasbenito/spatialrf: spatialrf: Easy spatial regression with random forest. Zenodo .
- Benito, B., 2021b. spatialrf: Spatial data analysis with random forest. URL: <https://github.com/BlasBenito/spatialRF>. accessed: 2023-04-05.
- Bian, L., 2025. Do microclimates matter? the health impacts of urban heat using fine-scale data. *Journal of Environmental Economics and Management* , 103191.

Biljecki, F., Chow, Y.S., 2022. Global Building Morphology Indicators. Computers, Environment and Urban Systems 95, 101809. doi:[10.1016/j.compenvurbsys.2022.101809](https://doi.org/10.1016/j.compenvurbsys.2022.101809).

Castro, E., Liu, A., Wei, Y., Kosheleva, A., Schwartz, J., 2024. Modification of the pm2.5-and extreme heat-mortality relationships by historical redlining: a case-crossover study in thirteen us states. Environmental Health 23, 16.

Chen, C., Li, D., Keenan, T.F., 2021. Enhanced surface urban heat islands due to divergent urban-rural greening trends. Environmental Research Letters 16, 124071.

Chen, K., Boomsma, J., Holmes, H.A., 2023. A multiscale analysis of heatwaves and urban heat islands in the western us during the summer of 2021. Scientific Reports 13, 9570.

Chen, Z., Yu, B., Yang, C., Zhou, Y., Qian, X., Wang, C., Wu, B., Wu, J., 2020. An extended time-series (2000–2018) of global npp-viirs-like nighttime light data from a cross-sensor calibration. Earth System Science Data Discussions 2020, 1–34.

Chew, L.W., Liu, X., Li, X.X., Norford, L.K., 2021. Interaction between heat wave and urban heat island: A case study in a tropical coastal city, singapore. Atmospheric Research 247, 105134.

Cui, F., Hamdi, R., Kuang, W., Yang, T., He, H., Termonia, P., De Maeyer, P., 2023. Interactions between the summer urban heat islands and heat waves in beijing during 2000–2018. Atmospheric Research 291, 106813.

Dai, Y., Liu, T., 2022. Spatiotemporal mechanism of urban heat island effects on human health—evidence from tianjin city of china. Frontiers in Ecology and Evolution 10, 1010400.

Du, H., Zhou, F., 2022. Mitigating extreme summer heat waves with the optimal water-cooling island effect based on remote sensing data from shanghai, china. International Journal of Environmental Research and Public Health 19, 9149.

ETH Zurich, 2024. Urban resilience: Climate resilience. <https://frs.ethz.ch/research/urban-resilience/climate-resilience.html>. Accessed: 2025-11-17.

Founda, D., Santamouris, M., 2017. Synergies between urban heat island and heat waves in athens (greece), during an extremely hot summer (2012). *Scientific reports* 7, 10973.

Gong, P., Li, X., Wang, J., Bai, Y., Chen, B., Hu, T., Liu, X., Xu, B., Yang, J., Zhang, W., et al., 2020. Annual maps of global artificial impervious area (gaia) between 1985 and 2018. *Remote Sensing of Environment* 236, 111510.

Govender, P., Sivakumar, V., 2020. Application of k-means and hierarchical clustering techniques for analysis of air pollution: A review (1980–2019). *Atmospheric pollution research* 11, 40–56.

Hathway, E., Sharples, S., 2012. The interaction of rivers and urban form in mitigating the urban heat island effect: A uk case study. *Building and environment* 58, 14–22.

He, B.J., Wang, J., Liu, H., Ulpiani, G., 2021. Localized synergies between heat waves and urban heat islands: Implications on human thermal comfort and urban heat management. *Environmental Research* 193, 110584.

He, Q., Cao, J., Saide, P.E., Ye, T., Wang, W., 2024. Unraveling the influence of satellite-observed land surface temperature on high-resolution mapping of ground-level ozone using interpretable machine learning. *Environmental Science & Technology* 58, 15938–15948.

He, X., Wang, J., Feng, J., Yan, Z., Miao, S., Zhang, Y., Xia, J., 2020. Observational and modeling study of interactions between urban heat island and heatwave in beijing. *Journal of Cleaner Production* 247, 119169.

He, Z., Wu, Z., Herzog, O., Hei, J., Li, L., Li, X., 2025. Compound health effects and risk assessment of extreme heat and ozone air pollution under climate change: A case study of 731 urban areas in china. *Sustainable Cities and Society* 119, 106084.

- Hirano, Y., Fujita, T., 2012. Evaluation of the impact of the urban heat island on residential and commercial energy consumption in tokyo. *Energy* 37, 371–383.
- Ho, J.Y., Shi, Y., Lau, K.K., Ng, E.Y., Ren, C., Goggins, W.B., 2023. Urban heat island effect-related mortality under extreme heat and non-extreme heat scenarios: A 2010–2019 case study in hong kong. *Science of the Total Environment* 858, 159791.
- Ip, A., Fong, S., Liu, E., 2010. Optimization for allocating bev recharging stations in urban areas by using hierarchical clustering, in: 2010 6th International conference on advanced information management and service (IMS), IEEE. pp. 460–465.
- Jiang, S., Lee, X., Wang, J., Wang, K., 2019. Amplified urban heat islands during heat wave periods. *Journal of Geophysical Research: Atmospheres* 124, 7797–7812.
- Jiang, Z., Huete, A.R., Didan, K., Miura, T., 2008. Development of a two-band enhanced vegetation index without a blue band. *Remote sensing of Environment* 112, 3833–3845.
- Joshi, M.Y., Rodler, A., Musy, M., Guernouti, S., Cools, M., Teller, J., 2022. Identifying urban morphological archetypes for microclimate studies using a clustering approach. *Building and Environment* 224, 109574.
- Kabisch, N., Remahne, F., Ilsemann, C., Fricke, L., 2023. The urban heat island under extreme heat conditions: a case study of hannover, germany. *Scientific Reports* 13, 23017.
- Kim, Y.H., Baik, J.J., 2004. Daily maximum urban heat island intensity in large cities of korea. *Theoretical and Applied Climatology* 79, 151–164.
- Lauer, A., Pausata, F.S., Leroyer, S., Argueso, D., 2023. Effect of urban heat island mitigation strategies on precipitation and temperature in montreal, canada: Case studies. *Plos Climate* 2, e0000196.
- Li, D., Bou-Zeid, E., 2013. Synergistic interactions between urban heat islands and heat waves: The impact in cities is larger than the sum of its parts. *Journal of applied Meteorology and Climatology* 52, 2051–2064.

Li, H., Liu, Y., Zhang, H., Xue, B., Li, W., 2021. Urban morphology in china: dataset development and spatial pattern characterization. *Sustainable Cities and Society* 71, 102981.

Li, H., Zhou, Y., Wang, X., Zhou, X., Zhang, H., Sodoudi, S., 2019. Quantifying urban heat island intensity and its physical mechanism using wrf/ucm. *Science of the Total Environment* 650, 3110–3119.

Li, Z., 2022. Extracting spatial effects from machine learning model using local interpretation method: An example of shap and xgboost. *Computers, Environment and Urban Systems* 96, 101845.

Liu, H.Q., Huete, A., 1995. A feedback based modification of the ndvi to minimize canopy background and atmospheric noise. *IEEE transactions on geoscience and remote sensing* 33, 457–465.

Luo, F., Yang, Y., Zong, L., Bi, X., 2023. The interactions between urban heat island and heat waves amplify urban warming in guangzhou, china: Roles of urban ventilation and local climate zones. *Frontiers in Environmental Science* 11, 1084473.

Magnaye, A.M.T., Kusaka, H., 2024. Potential effect of urbanization on extreme heat events in metro manila philippines using wrf-ucm. *Sustainable Cities and Society* 110, 105584.

McFeeters, S.K., 2013. Using the normalized difference water index (ndwi) within a geographic information system to detect swimming pools for mosquito abatement: a practical approach. *Remote Sensing* 5, 3544–3561.

Meteorological Service Singapore, 2023. Climate of Singapore. URL: <http://www.weather.gov.sg/climate-climate-of-singapore/>. accessed: 2023-04-03.

Molnar, C., Schratz, P., 2020. Package ‘iml’. R CRAN .

Mzid, N., Pignatti, S., Huang, W., Casa, R., 2021. An analysis of bare soil occurrence in arable croplands for remote sensing topsoil applications. *Remote Sensing* 13, 474.

Oke, T.R., Mills, G., Christen, A., Voogt, J.A., 2017. Urban climates. Cambridge university press.

Peel, M.C., Finlayson, B.L., McMahon, T.A., 2007. Updated world map of the köppen-geiger climate classification. *Hydrology and earth system sciences* 11, 1633–1644.

Coughlan de Perez, E., Arrighi, J., Marunye, J., 2023. Challenging the universality of heatwave definitions: gridded temperature discrepancies across climate regions. *Climatic Change* 176, 167.

Perkins-Kirkpatrick, S., Lewis, S., 2020. Increasing trends in regional heatwaves. *Nature communications* 11, 3357.

Perkins-Kirkpatrick, S.E., Gibson, P.B., 2017. Changes in regional heatwave characteristics as a function of increasing global temperature. *Scientific Reports* 7, 12256.

Qiu, W., Yan, X., 2020. The trend of heatwave events in the northern hemisphere. *Physics and Chemistry of the Earth, Parts A/B/C* 116, 102855.

Rajeswari, J., Fountoukis, C., Siddique, A., Moosakutty, S., Mohieldeen, Y., Ayoub, M.A., Alfarra, M.R., 2024. Urban heat island phenomenon in a desert, coastal city: The impact of urbanization. *Urban Climate* 56, 102016.

Richard, Y., Pohl, B., Rega, M., Pergaud, J., Thévenin, T., Emery, J., Dudek, J., Vairet, T., Zito, S., Chateau-Smith, C., 2021. Is urban heat island intensity higher during hot spells and heat waves (dijon, france, 2014–2019)? *Urban Climate* 35, 100747.

Rikimaru, A., Roy, P., Miyatake, S., et al., 2002. Tropical forest cover density mapping. *Tropical ecology* 43, 39–47.

Rizvi, S.H., Alam, K., Iqbal, M.J., 2019. Spatio-temporal variations in urban heat island and its interaction with heat wave. *Journal of Atmospheric and Solar-Terrestrial Physics* 185, 50–57.

Rizwan, A.M., Dennis, L.Y., Chunho, L., 2008. A review on the generation, determination and mitigation of urban heat island. *Journal of environmental sciences* 20, 120–128.

- Rogers, C.D., Gallant, A.J., Tapper, N.J., 2019. Is the urban heat island exacerbated during heatwaves in southern australian cities? *Theoretical and applied climatology* 137, 441–457.
- Russo, E., Domeisen, D.I., 2023. Increasing intensity of extreme heatwaves: the crucial role of metrics. *Geophysical Research Letters* 50, e2023GL103540.
- Shahmohamadi, P., Che-Ani, A., Etessam, I., Maulud, K., Tawil, N., 2011. Healthy environment: the need to mitigate urban heat island effects on human health. *Procedia Engineering* 20, 61–70.
- Shreevastava, A., Prasanth, S., Ramamurthy, P., Rao, P.S.C., 2021. Scale-dependent response of the urban heat island to the european heatwave of 2018. *Environmental Research Letters* 16, 104021.
- Singh, M., Sharston, R., 2022. Quantifying the dualistic nature of urban heat island effect (uhi) on building energy consumption. *Energy and Buildings* 255, 111649.
- Štrumbelj, E., Kononenko, I., 2014. Explaining prediction models and individual predictions with feature contributions. *Knowledge and information systems* 41, 647–665.
- Su, H., Qi, Z., Wang, Q., 2025. Impacts of land use characteristics on extreme heat events: Insights from explainable machine learning model. *Sustainable Cities and Society* , 106139.
- Sun, D., Hu, C., Wang, Y., Wang, Z., Zhang, J., 2021. Examining spatio-temporal characteristics of urban heat islands and factors driving them in hangzhou, china. *IEEE Journal of Selected Topics in Applied Earth Observations and Remote Sensing* 14, 8316–8325.
- Syed Mahbar, S.F., Kusaka, H., 2024. Synergistic interactions between urban heat islands and heat waves in the greater kuala lumpur and surrounding areas. *International Journal of Climatology* 44, 4886–4906.

- Tan, J., Zheng, Y., Tang, X., Guo, C., Li, L., Song, G., Zhen, X., Yuan, D., Kalkstein, A.J., Li, F., et al., 2010. The urban heat island and its impact on heat waves and human health in shanghai. *International journal of biometeorology* 54, 75–84.
- Tang, L., Gao, J., Ren, C., Zhang, X., Yang, X., Kan, Z., 2019. Detecting and evaluating urban clusters with spatiotemporal big data. *Sensors* 19, 461.
- Walther, C., Olonscheck, M., 2016. Analysing heat exposure in two german cities by using meteorological data from both within and outside the urban area. *Meteorological Applications* 23, 541–553.
- Wang, G., Zhang, Q., Luo, M., Singh, V.P., Xu, C.Y., 2022. Fractional contribution of global warming and regional urbanization to intensifying regional heatwaves across eurasia. *Climate Dynamics* , 1–17.
- Wei, C., Chen, W., Lu, Y., Blaschke, T., Peng, J., Xue, D., 2021. Synergies between urban heat island and urban heat wave effects in 9 global mega-regions from 2003 to 2020. *Remote Sensing* 14, 70.
- Wu, S., Luo, M., Zhao, R., Li, J., Sun, P., Liu, Z., Wang, X., Wang, P., Zhang, H., 2023. Local mechanisms for global daytime, nighttime, and compound heatwaves. *NPJ Climate and Atmospheric Science* 6, 36.
- Xi, Z., Li, C., Zhou, L., Yang, H., Burghardt, R., 2023. Built environment influences on urban climate resilience: Evidence from extreme heat events in macau. *Science of The Total Environment* 859, 160270.
- Xue, J., Su, B., 2017. Significant remote sensing vegetation indices: A review of developments and applications. *Journal of sensors* 2017, 1353691.
- Yang, W., Li, Y., Liu, Y., Fan, P., Yue, W., 2024. Environmental factors for outdoor jogging in beijing: Insights from using explainable spatial machine learning and massive trajectory data. *Landscape and urban planning* 243, 104969.

Yang, Y., Yuan, Y., Han, Z., Liu, G., 2022. Interpretability analysis for thermal sensation machine learning models: An exploration based on the shap approach. *Indoor air* 32, e12984.

Yu, J., Kumar, A., Pattnayak, K.C., Obbard, J., Moise, A.F., 2023. Characteristics of compound climate extremes and impacts in singapore, 1985–2020. *Climate* 11, 58.

Zhang, T., Zhou, Y., Zhao, K., Zhu, Z., Chen, G., Hu, J., Wang, L., 2022. A global dataset of daily near-surface air temperature at 1-km resolution (2003–2020). *Earth System Science Data Discussions* 2022, 1–18.

Zhang, T., Zhou, Y., Zhu, Z., Li, X., Asrar, G.R., 2021. A global seamless 1 km resolution daily land surface temperature dataset (2003–2020). *Earth System Science Data Discussions* 2021, 1–16.

Zhao, L., Oppenheimer, M., Zhu, Q., Baldwin, J.W., Ebi, K.L., Bou-Zeid, E., Guan, K., Liu, X., 2018. Interactions between urban heat islands and heat waves. *Environmental research letters* 13, 034003.

Zheng, Y., Ren, C., Xu, Y., Wang, R., Ho, J., Lau, K., Ng, E., 2018. Gis-based mapping of local climate zone in the high-density city of hong kong. *urban clim.* 24, 419–448.

Zhou, S., Xu, Z., Liu, F., 2016. Method for determining the optimal number of clusters based on agglomerative hierarchical clustering. *IEEE transactions on neural networks and learning systems* 28, 3007–3017.

Zhu, S., Dai, Q., Zhao, B., Shao, J., 2020. Assessment of population exposure to urban flood at the building scale. *Water* 12, 3253.

Zong, L., Liu, S., Yang, Y., Ren, G., Yu, M., Zhang, Y., Li, Y., 2021. Synergistic influence of local climate zones and wind speeds on the urban heat island and heat waves in the megacity of beijing, china. *Frontiers in Earth Science* 9, 673786.